# SNIa Cosmology Analysis Results from Simulated LSST Images: From Difference Imaging to Constraints on Dark Energy

B. O. Sánchez[1] , R. Kessler[2,3] , D. Scolnic[1] , R. Armstrong[4] , R. Biswas[5] , J. Bogart[6] , J. Chiang[6,7] ,
J. Cohen-Tanugi[8,9] , D. Fouchez[10] , Ph. Gris[9] , K. Heitmann[11] , R. Hložek[12] , S. Jha[13] , H. Kelly[6,7] , S. Liu[14] ,
G. Narayan[15,16] , B. Racine[10] , E. Rykoff[6] , M. Sullivan[17] , C. W. Walter[1] , and W. M. Wood-Vasey[14]
The LSST Dark Energy Science Collaboration (DESC)

[1] Department of Physics, Duke University, 120 Science Dr., Durham, NC 27708, USA; bruno.sanchez@duke.edu
[2] Department of Astronomy and Astrophysics, University of Chicago, Chicago, IL 60637, USA
[3] Kavli Institute for Cosmological Physics, University of Chicago, Chicago, IL 60637, USA
[4] Lawrence Livermore National Laboratory, 7000 East Ave., Livermore, CA 94550-9234, USA
[5] Stockholm University, Universitetsvägen 10, SE-114 18 Stockholm, Sweden
[6] SLAC National Accelerator Laboratory, 2575 Sand Hill Road, Menlo Park, CA, 94025, USA
[7] Kavli Institute for Particle Astrophysics and Cosmology, Stanford University, Stanford CA 94305, USA
[8] Laboratoire Univers et Particules de Montpellier, Place Eugène Bataillon—CC 72, F-34095 Montpellier Cedex 05, France
[9] LPC, IN2P3/CNRS, Université Clermont Auvergne, F-63000 Clermont-Ferrand, France
[10] Centre de Physique des Particules de Marseille, 163, avenue de Luminy Case 902 F-13288 Marseille cedex 09, France
[11] HEP Division, Argonne National Laboratory, 9700 S. Cass Ave., Lemont, IL 60439, USA
[12] University of Toronto, 27 King's College Cir., Toronto, ON M5S, Canada
[13] Department of Physics and Astronomy, Rutgers University, Piscataway, NJ 08854, USA
[14] Pittsburgh Particle Physics, Astrophysics, and Cosmology Center (PITT PACC). Department of Physics and Astronomy, University of Pittsburgh, 4200 Fifth Ave.,
Pittsburgh, PA 15260, USA
[15] Department of Astronomy, University of Illinois at Urbana-Champaign, Urbana, IL 61801, USA
[16] Center for AstroPhysical Surveys (CAPS), National Center for Supercomputing Applications (NCSA), University of Illinois at Urbana-Champaign, Urbana IL
61801, USA
[17] School of Physics and Astronomy, University of Southampton, University Rd., Southampton, SO17 1BJ, UK

## Abstract

The Vera Rubin Observatory Legacy Survey of Space and Time (LSST) is expected to process $\sim 10^6$ transient detections per night. For precision measurements of cosmological parameters and rates, it is critical to understand the detection efficiency, magnitude limits, artifact contamination levels, and biases in the selection and photometry. Here we rigorously test the LSST Difference Image Analysis (DIA) pipeline using simulated images from the Rubin Observatory LSST Dark Energy Science Collaboration Data Challenge (DC2) simulation for the Wide-Fast-Deep survey area. DC2 is the first large-scale ($300\,\mathrm{deg}^2$) image simulation of a transient survey that includes realistic cadence, variable observing conditions, and CCD image artifacts. We analyze $\sim 15\,\mathrm{deg}^2$ of DC2 over a 5 yr time span in which artificial point sources from Type Ia supernova (SNIa) light curves have been overlaid onto the images. The magnitude limits per filter are $u = 23.66$ mag, $g = 24.69$ mag, $r = 24.06$ mag, $i = 23.45$ mag, $z = 22.54$ mag, and $y = 21.62$ mag. The artifact contamination levels are $\sim 90\%$ of all detections, corresponding to $\sim 1000$ artifacts $\mathrm{deg}^{-2}$ in $g$ band, and falling to $300\,\mathrm{deg}^{-2}$ in $y$ band. The photometry has biases $<1\%$ for magnitudes $19.5 < m < 23$. Our DIA performance on simulated images is similar to that of the Dark Energy Survey difference-imaging pipeline on real images. We also characterize DC2 image properties to produce catalog-level simulations needed for distance bias corrections. We find good agreement between DC2 data and simulations for distributions of signal-to-noise ratio, redshift, and fitted light-curve properties. Applying a realistic SNIa cosmology analysis for redshifts $z < 1$, we recover the input cosmology parameters to within statistical uncertainties.

## 1. Introduction

The Vera C. Rubin Observatory Legacy Survey of Space and Time (LSST;[18] Ivezić et al. 2019) is expected to soon begin operations and acquire images over 10 yr. This survey will use the Simonyi Survey Telescope at Rubin Observatory, which is an 8.4 m class[19] telescope with a 3.2 gigapixel camera, yielding a $9.6\,\mathrm{deg}^2$ field of view. The Rubin Observatory LSST camera design includes *ugrizy* filters, and the expected $5\sigma$ $r$-band depth is $>24$ (AB system) in a single 30 s visit, where each visit is composed of two 15 s exposures. The instrument and the survey strategy have been optimized toward obtaining repeated observation of $\sim 20,000\,\mathrm{deg}^2$ of the sky over 10 yr.

---

[18] http://www.lsst.org

---

[19] 6.7 m of effective collecting area.

LSST will explore a broad range of research fields in astrophysics (LSST Science Collaboration et al. 2009); the main science objectives are the study of solar system dynamics, mapping the Milky Way structure, and probing dark matter and dark energy. Many of these science goals rely on the discovery of transient sources, and the expected number of transient detections from all astrophysical variability sources is $\sim 10^6$ per night[20] (Ridgway et al. 2014; Ivezić et al. 2019; Graham et al. 2020), an unprecedented rate when comparing to precursor surveys. Past transient surveys have focused on either low redshift ($z < 0.1$) using shallow/wide area strategies or higher redshift using deep/limited area strategies (see Scolnic et al. 2018a for a review). The unique capabilities of LSST enable survey strategies using wide areas with deep images. To discover transients and measure their light curves, the LSST project has developed Difference Image Analysis (DIA) software components. The Rubin Observatory LSST Dark Energy Science Collaboration (DESC[21]) used these components to develop an orchestration software layer called `dia_pipe`.[22] In this paper, we make the first evaluation of this pipeline by analyzing simulated images.

Type Ia supernovae (SNeIa) are transient events that are used as cosmological probes to measure the expansion history of the universe and in particular the dark energy equation of state $w$ (and its cosmic evolution parameterized by $w_a$; The LSST Dark Energy Science Collaboration (DESC) Science Roadmap 2019). LSST is expected to increase the SNIa sample size by up to a factor of 100 compared to previous samples (Betoule et al. 2014; Sako et al. 2018; Scolnic et al. 2018a; Jones et al. 2019). Furthermore, the survey will yield the discovery of SNeIa using a single instrument with redshifts up to $z \sim 1.2$. The requirements on systematic uncertainties from the SNIa cosmology analysis are detailed in The LSST Dark Energy Science Collaboration et al. (2018); these requirements include photometric precision at the few-millimagnitude level and accurately determined selection biases.

To rigorously test analysis pipelines before the pre-survey commissioning period, DESC has generated a large and comprehensive set of image simulations known as Data Challenge 2 (DC2; LSST Dark Energy Science Collaboration et al. 2020; Sánchez et al. 2020). Each DC2 image is based on models of the LSST instrument and expected observing conditions at the summit (sky noise and point-spread function (PSF)), along with realistic catalogs of galaxies and SN light curves. The full DC2 area covers $300\,\mathrm{deg}^2$ of the Wide-Fast-Deep (WFD) survey and includes injected point sources of SNeIa with an average cadence of 3 days (15 days in each filter). Using a DC2 subset of $15\,\mathrm{deg}^2$, we have processed the raw CCD pixels with DIA to characterize SNIa transient finding, photometric precision, and selection effects. In addition, we treat DC2 like real data and perform a cosmology analysis that includes light-curve fitting, bias-correcting distances, and fitting for cosmological parameters $w$ and $\Omega_M$. This pixel-to-cosmology test is a critical part of evaluating `dia_pipe` readiness for survey operations.

The layout of this work is the following. In Section 2 we explain the DC2 data set used, and in Section 3 we give details on the analysis and the techniques implemented. Section 4 shows our results on DC2 data processing, and Section 5 lists performance metric scores obtained for transient detection and cosmology fitting. In Section 6 we discuss our results and compare them to previously reported analysis. The final discussion and conclusions are presented in Section 7.

## 2. The DC2 Data Set

The DC2 is a broad DESC effort to create and process simulated LSST images based on modeling galaxies and transients in the universe (LSST Dark Energy Science Collaboration et al. 2020). The simulation is composed of observations spanning a sky area of $300\,\mathrm{deg}^2$ during 5 yr of survey operations. The simulated data include the expected instrumental signatures from the LSST Camera and the atmospheric effects in all six optical bands *ugrizy*. DC2 contains stars, galaxies, and astrophysical effects such as clustering, cosmic web/structure formation, and gravitational lensing effects such as cosmic shear. DC2 also includes variable stars, transient variability from SNeIa,[23] active galactic nucleus (AGN) galaxies, and strong-lensed SNeIa.

DC2 used the state-of-the-art *N*-body simulation *Outer Rim* (Heitmann et al. 2019). The cosmological parameters used to create *Outer Rim* are consistent with WMAP-7 (Komatsu et al. 2011). From this gravity-only simulation, the `cosmoDC2` mock catalog (Korytov et al. 2019) is created; it covers $440\,\mathrm{deg}^2$ of sky area up to a redshift of $z = 3$. CosmoDC2 contains more than 500 properties for each galaxy, including stellar and halo mass, shape, spectral energy density (SED), central black hole parameters, AGN activity, and environment-related quantities such as the full gravitational shear and convergence maps of the sky, which give the observed shape of each galaxy.

In this work we use Run 2.2i WFD images with an average transient cadence of 3 days between observations. DC2 images were produced with the image simulation software `imSim`[24] that imprints observing conditions and instrumental signatures using a model of the LSSTCam. The observing conditions, which include sky noise, PSF, zero-point, and dithering, are based on the `minion_1016`[25] observing strategy produced with the operations simulator software `OpSim`.[26] Each object SED is attenuated from a calculation of Galactic dust extinction and atmospheric effects that includes differential chromatic refraction. Effects from the CCD readout electronics are also simulated, including charge repulsion effects and saturation. Each simulated visit illuminates 189 $4k \times 4k$ CCD detectors (3 billion pixels) covering almost $10\,\mathrm{deg}^2$, with a plate scale of $0\farcs2\,\mathrm{pixel}^{-1}$.

A summary of the DC2 SNIa properties is shown in Table 1. For SNeIa, the rest-frame SED is computed with the SALT2 model (Guy et al. 2010; Betoule et al. 2014). Since the original SED model covers only the *g* and *r* bands in the rest frame, we use a wavelength-extended model (Pierel et al. 2018) that covers all of the LSST bands. For `imSim` to run properly, we include an additional modification that prevents negative UV spectral fluxes. The properties of each SNIa in DC2 are determined by the following SALT2 parameters: redshift ($z$), time at peak brightness ($t_0$), stretch ($x_1$), color ($c$), and amplitude ($x_0$). Each redshift is randomly selected from a

---

**Table 1**
SNIa Properties Used in DC2 Simulations

| DC2 SNIa Property | |
| --- | --- |
| Light-curve model | SALT2-Extended + 0.15 mag offset[a] (Pierel et al. 2018) |
| Rate model | $r_v(z) = 2.5 \times 10^{-5}(1 + z)^{1.5}$ Mpc$^3$ yr$^{-1}$ (Dilday et al. 2008) |
| Intrinsic scatter | $\sigma_{int} = 0.15$ mag |
| Host correlation | None |
| Stretch population | $\bar{x}_1 = 0.873$, $\sigma_+ = 1.43$, $\sigma_- = 0.359$, Range = $[-3.0, 2.0]$ |
| Color population | $\bar{c} = -0.048$, $\sigma_+ = 0.043$, $\sigma_- = 0.097$, Range = $[\pm 0.3]$ |
| Luminosity parameters | $\alpha = 0.137$, $\beta = 3.21$ |

**Note.**
[a] This offset was a mistake in the DC2 generation and is included in the simulations for bias corrections.

volumetric rate, $r_v(z) = 2.5 \times 10^{-5}(1 + z)^{1.5}$ Mpc$^3$ yr$^{-1}$ (Dilday et al. 2008). The $t_0$ value is randomly selected within the 5 yr DC2 time span. Each SNIa includes an intrinsic scatter drawn from a Gaussian distribution with $\sigma = 0.15$ mag; a coherent mag fluctuation is applied at all SNIa phases and wavelengths. The SALT2 parameters $x_1$ and $c$ were each drawn from an asymmetric Gaussian distribution with parameters shown in Table 1. The amplitude $x_0$ is computed from the SALT2 parameters and the luminosity distance. The luminosity parameters $\alpha$ and $\beta$ were set to 0.137 and 3.21, respectively.

Correlations between the SNIa and host galaxy properties were not included in the simulations. SNe were assigned to a galaxy using an occupation probability proxy of stellar mass. For host galaxies of SNeIa, the cosmoDC2 stellar mass distribution peaks at $\sim 10^{11}\ M_\odot$, which is $\sim 5$ dex higher than the typical mass of field galaxies (see Figure 5 in LSST Dark Energy Science Collaboration et al. 2020). A total of 10% of SNeIa are assigned to be "hostless" in order to provide a control sample of isolated transients.

DC2 images are processed by the LSST pipelines, which organize image data in sets of *tracts* and *patches* for operational purposes. Each 2.56 deg$^2$ tract is a square containing $7 \times 7$ patches that share a common World Coordinate System (WCS) projection. This sky map organization is used for image co-addition grid resampling, database access and image data manipulation, DIA processing, and template creation. Each DC2 patch contains $4100 \times 4100$ pixels (roughly the size of a CCD) with a scale of $0\rlap{.}''2$. To avoid missing area due to edge effects, patches overlap with their neighbors by 100 pixels, and tracts overlap by $1'$.

In this work, we select a 15 deg$^2$ area from the DC2 WFD (hereafter called "DC2-SNIa" area) that includes 1967 LSSTcam visit observations and 105,942 CCD images. We select SNeIa with redshifts $z \leqslant 1.0$, which includes the full range of cosmologically useful SNeIa that will be discovered in the WFD (The LSST Dark Energy Science Collaboration et al. 2018). We discard objects $<65''$ from the edges of the DC2-SNIa area in order to avoid subtraction artifacts from template overlapping issues. DC2-SNIa contains 5884 SNeIa, and Figure 1 shows distributions of redshift and SALT2 parameters. Figure 2 shows the DC2-SNIa sky area used in this
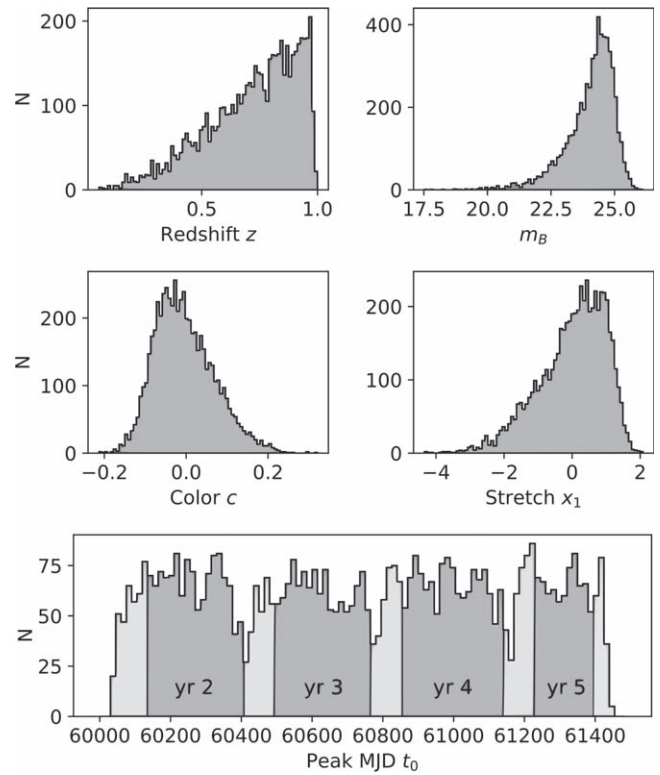


**Figure 1.** Distribution of redshift and SALT2 model parameters for DC2 SNeIa. The light-gray regions (bottom panel) are for events whose peak brightness occurs outside a season of observations.

work, illustrating the tracts and patches used, and the locations of analyzed SNeIa.

The DC2 simulation choices were made several years ago and cannot be altered without an enormous effort to regenerate DC2. While some of these choices are no longer based on the most current measurements, these choices are nonetheless consistent with current observations.

## 3. Analysis

Here we describe the DIA LSST pipeline framework and SNIa-cosmological analysis.

### 3.1. DIA Pipeline Framework

The Rubin Observatory Data Management team has developed a state-of-the-art set of software tools for CCD data reduction that contains several routines for image processing, such as image co-addition, flux measurements, etc. This image processing framework, named "LSST Science Pipelines,"[27] is open source and can be used on any optical and infrared survey data set. DESC uses the LSST pipeline system to remove instrumental signatures from DC2 images (e.g., electronic readout bias, dark current, illumination gradients), to calibrate images, and to obtain a WCS solution.

For transient detection, DESC has developed a specific pipeline package dia_pipe that uses LSST Science Pipelines' image processing tools, including DIA routines. The central concept of DIA is to compare two images of the same sky area taken at different times and detect sources that change in brightness. Each image has different properties (PSF, sky
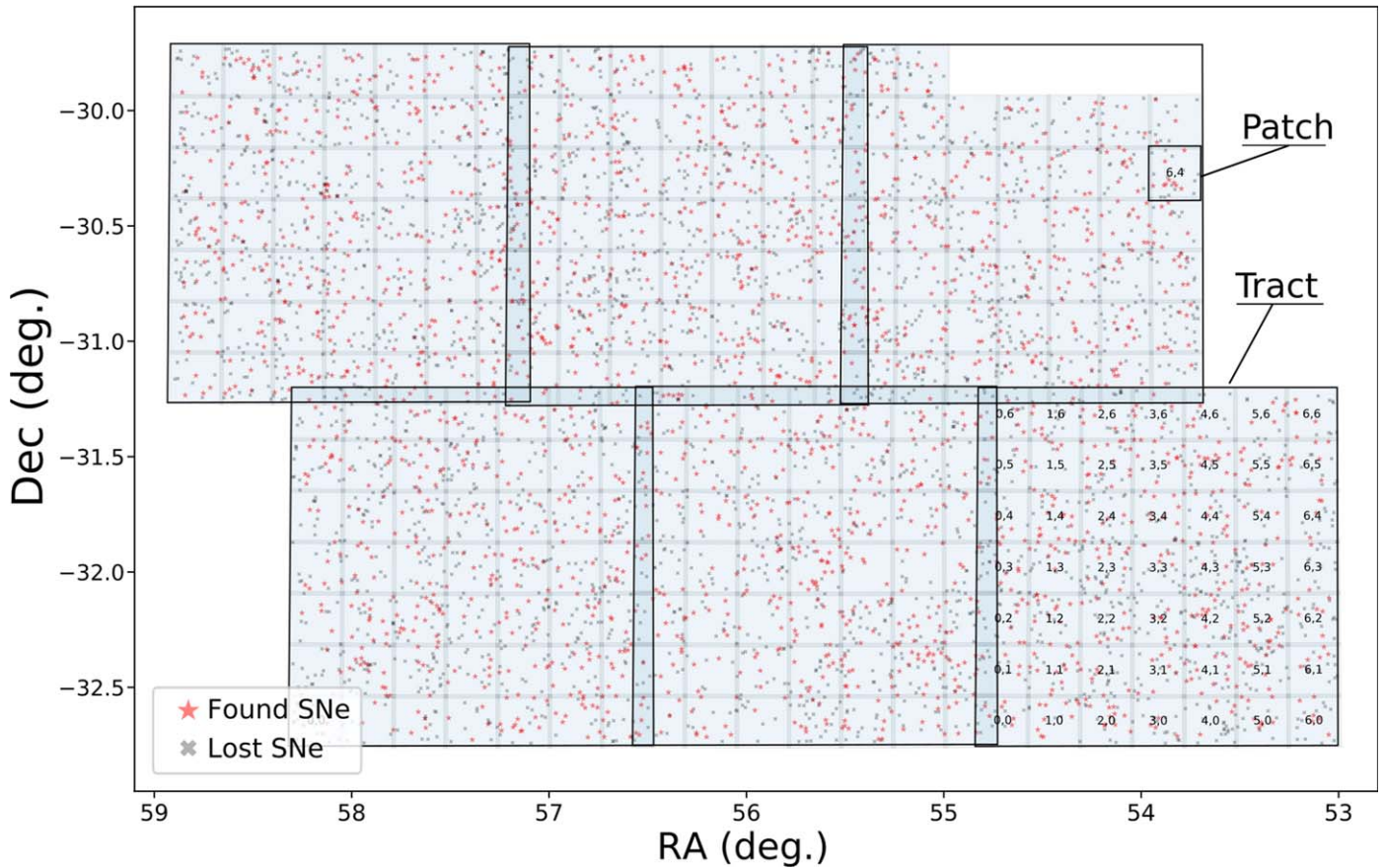
---

[27] https://pipelines.lsst.io

**Figure 2.** DC2-SNIa sky area. Small squares indicate patches, and large squares are tracts. Detected and undetected SNe are shown as red stars and gray crosses, respectively. In light blue we show used DC2 patches, and we include the patch numbers for only one of the tracts.

noise, zero-point, etc.), and the subtraction accounts for these effects. DIA uses a co-added reference image (*template*) and one recently observed *search image* on which we want to find variability. The reference image is constructed by stacking a subset of archival images taken in exceptional observing conditions with low sky noise, small PSF size, and high atmosphere transparency (more details in Section 4.1). Since these templates are built from many individual observations, pixels with artifacts (e.g., moving object trails, cosmic rays, CCD blooming and bleeding) are rejected during the co-addition process. In this work, DIA is based on the Alard & Lupton (1998, hereafter A&L) technique, which uses a kernel to transform the template image such that its pixel locations, orientation, and PSF match the search image.

The dia_pipe stages are illustrated in the top panel of Figure 3 and briefly described below:

1. *Instrumental signature removal and calibration*: Simulated images, including calibration frames (dark current, bias, and flat-field exposures) are ingested to perform Instrumental Signature Removal (ISR) and image calibration, resulting in a repository of calibrated image exposures called "*Calexp's*."

2. *Template co-addition*: From the Calexp repository, the best 40 images per band are selected from the first season (Y1), based on seeing ($<1\rlap{.}''3$), low sky noise, and significant overlap with DC2 patches. These images are co-added to build templates using a weighted mean

procedure, and pixel weights are estimated using the inverse variance.

3. *DIA*: The A&L image subtraction algorithm is run on images from seasons 2–5, which produces difference images. The DIA kernel basis is composed of three Gaussians, with an adaptive spatially varying size to accommodate varying PSF sizes. The basis components also vary spatially. Next, source detection is run on each difference image to obtain a catalog of DIA single-visit detections, called diaSource. To avoid artifacts near CCD edges, detections within 16 pixels of an image edge are discarded; this cut is about $3\times$ larger than the typical PSF–FWHM size. At least one corner of each search image is required to overlap a template image within $65''$ of the edge.

4. *Association*: a candidate-association algorithm creates diaObjects from one or more diaSources that match spatially within $0\rlap{.}''5$. This cut radius is much larger than the average astrometric precision of DC2 calibration (see Figure 13 of LSST Dark Energy Science Collaboration et al. 2020). As each diaSource is added to a diaObject, the average R.A. and decl. coordinate of the diaObject is updated.

5. *Forced photometry*: For each diaObject, forced PSF photometry is performed at the location of the object for all overlapping images, regardless of whether there was a diaSource detection. The PSF is determined from the *Calexp* image. The collection of forced photometry fluxes
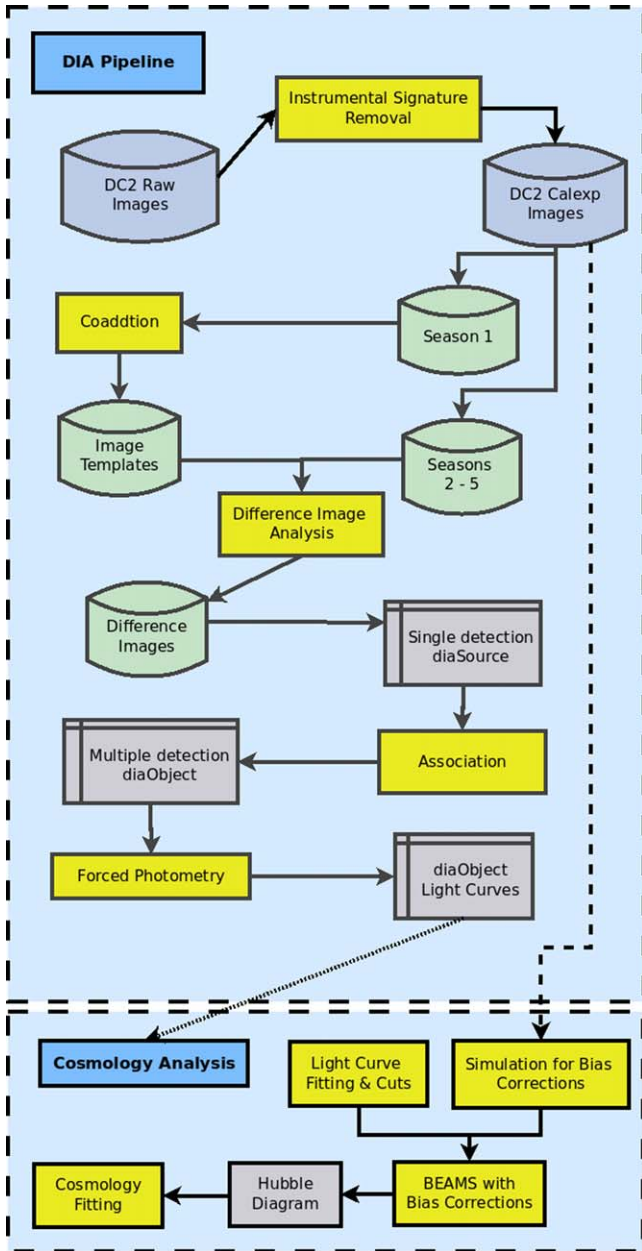
**Figure 3.** Diagram of `dia_pipe` and LSST Science Pipelines (top box). Each processing step (yellow boxes) takes an image (green cylinders) or catalog data (gray tables) and produces new images or catalogs. Additionally, we show connections to the cosmology analysis (bottom box).

and uncertainties for each `diaObject` composes the light curve used in the cosmology analysis (Section 3.3).

### 3.2. DIA Validation

Before using the light curves for the cosmology analysis, we perform several validation checks on the performance of the DIA steps explained in Section 3.1. These validation checks include the following:

1. Template quality (depth and PSF size).
2. Efficiency versus signal-to-noise ratio (S/N).
3. Detection depth per band.
4. Artifact contamination level.
5. Photometric precision for fluxes.

6. Photometric uncertainty correlation with surface brightness.
7. Photometric flux-outlier fractions.

### 3.3. Cosmology Analysis

Here we describe a cosmology analysis that combines the DC2 light curves, obtained with the DIA pipeline framework, together with a simulated LSST WFD low-redshift (SimLow-z) sample generated with the SNANA simulation. The SimLow-z sample covers a redshift range of $z < 0.08$ with an assumed spectroscopic selection efficiency of 100%. The "DC2+Sim-Low-z" analysis includes light-curve fitting to standardize the SNIa brightness, a Monte Carlo simulation to correct for selection effects, a global fit to produce a bias-corrected Hubble diagram, and a $w$CDM fit to estimate $w$ and $\Omega_M$ (see bottom panel of Figure 3). We closely follow the procedures used in the analyses for Pantheon (Scolnic et al. 2018b), PS1 (Rest et al. 2014; Jones et al. 2018), and DES (Brout et al. 2019).

To the extent possible, we treat DC2 light-curve data as real data by not using underlying truth information. However, there are five caveats where truth information is used: (1) We do not use DC2 data to train the SALT2 model, nor to measure the true color and stretch populations; instead, we use the known SALT2 model for light-curve fitting, and we use the known SALT2 and population model for the bias correction simulations. (2) We select light curves from `diaObjects` that match true DC2 SNeIa, and thus our DC2 sample corresponds to a spectroscopically confirmed sample without contamination from other SN types. (3) We use the true DC2 redshifts and thus assume accurate redshifts from either the SN or correctly matched host galaxy. (4) To characterize DIA detection efficiency versus S/N, we use the same DC2 light-curve data as in the analysis; for future LSST analysis of real data, there will be a separate data stream of fake sources to measure this DIA property. (5) For simulated bias corrections, we use the same rate model as in DC2 (Dilday et al. 2008).

The analysis stages described below use programs from the Supernova Analysis (SNANA; Kessler et al. 2009) software package[28]:

1. *Light-curve fitting on data*: We use the SALT2-Extended (Pierel et al. 2018) light-curve model, the same model used to generate DC2 SNeIa, and fit for $t_0$, $x_0$, $x_1$, and $c$ parameters and their covariances. We impose the following selection requirements (cuts) based on previous cosmology analyses:
   (a) at least one detection (Section 5.1) in any passband;
   (b) maximum $S/N > 4$ in at least three separate passbands;
   (c) fitted $|x_1| < 3$, and $0 < \sigma_{x_1} < 2$;
   (d) fitted $|c| < 0.3$;
   (e) fitted peak MJD uncertainty $< 3$ days;
   (f) fit probability ($P_{fit}$), computed from $\chi^2$ and the number of degrees of freedom (NDOF), satisfies $P_{fit} > 0.05$;
   (g) at least one observation before $t_0$, and another 10 days after $t_0$ in the rest frame;
   (h) require valid bias correction in BBC (see Hubble diagram determination below).

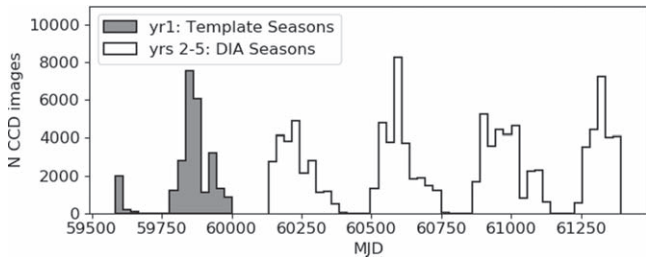In addition to the SN selection cuts, we select observations that satisfy the following:

---

**Figure 4.** Distribution of observation dates (MJD) from DC2 images spanning five seasons. The first season (shaded) is used for templates.

(a) no interpolated pixels near the center;

(b) rest-frame time is between $t_0 - 15$ and $t_0 + 45$ days.

2. *Simulation for bias corrections*: To prepare for distance bias corrections, we generate a catalog-level simulation as described in Kessler et al. (2019). We use DC2 DIA data to determine a cadence library (Section 6.1 of Kessler et al. 2019), detection efficiency versus S/N for each band, and flux uncertainty corrections. The same cadence library and detection efficiency were used to simulate both the DC2 and the SimLow-z samples.

3. *Hubble diagram*: We use "BEAMS with Bias Corrections" (BBC; Kessler & Scolnic 2017) to determine a bias-corrected Hubble diagram in nine redshift bins and to determine nuisance parameters: stretch−luminosity correlation $\alpha$, color−luminosity correlation $\beta$, and intrinsic scatter $\sigma_{int}$.

4. *Cosmology fitting*: We fit for $w$ and $\Omega_M$ using a fast minimization program (wFit) that combines the DC2 +SimLow-z SNIa Hubble diagram with a cosmic microwave background (CMB) prior using the $R(z_*)$ shift parameter (see, e.g., Equation (69) in Komatsu et al. 2009). To avoid bias from the prior, $R(z_*)$ is computed from the DC2 cosmology parameters. To have CMB constraining power similar to that of Planck (Ade et al. 2016), we tuned the $R$-uncertainty, $\sigma_R = 0.007$, as follows. Since the Pantheon (Scolnic et al. 2018b) and DES-SN3YR (Abbott et al. 2019)[29] results include the full Planck likelihood as a prior, we fit their publicly available SNIa Hubble diagrams and covariance matrix with wFit and tune $\sigma_R$ to match the published $w$-uncertainties of 0.041 and 0.059 for Panthoen and DES-SN3YR, respectively.

## 4. Data Processing Results

We processed DC2 image data using six tracts, which comprises a sky area of 15 deg$^2$ during five observing year-seasons. We used the first year for template creation (Figure 4) and the remaining 4 yr (hereafter called DIA seasons) for image subtractions, creating a total of $\sim$106 k DIA images in all LSST filters *ugrizy*.

### 4.1. Template Creation

We show the distributions of the number of images used per template in Figure 5 in a boxplot format. The distributions peak near 40, and they all have a tail extending down to $\sim$15 images owing to insufficient overlap with the corresponding patch area.

---

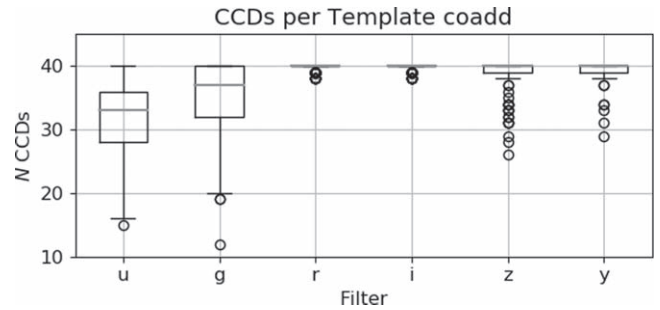29 https://des.ncsa.illinois.edu/releases/sn



**Figure 5.** Distribution boxplots of the number of CCD sensors used per template image (one template per patch, of roughly 14′ a side). Boxes and whiskers represent $1\sigma$ and $3\sigma$ width of distribution, with center line indicating the mean value. Outliers are marked with open circles.

For the template and DIA season images, photometric properties of PSF and $5\sigma$ limiting magnitude depth ($m_{5\sigma}$) are listed in Table 2.

We compare $m_{5\sigma}$ for templates and DIA seasons in Figure 6. The template depth is $\sim$ 1 mag deeper than DIA season images. Figure 7 shows that the PSF distribution for templates is generally smaller and narrower compared to DIA season visits. The exception is $u$ band, where the template PSF is larger than for DIA season visits because weather fluctuations caused the first-season PSF distribution to be larger than that for the other seasons.

### 4.2. Image Differences

Our final DIA sample contains a total number of 1967 visits, or 105,942 individual images. In Figure 8, we show an example of the DIA process from DC2.

## 5. Performance Metric Results

Here we characterize the performance of DIA detections, matching, photometric precision, and level of nonastrophysical detections (subtraction artifacts). For the cosmology analysis, we define metrics based on data-sim distribution overlays of properties of the light curves, $z$-dependent Hubble diagram bias, and fitted cosmology parameters.

### 5.1. DIA on Single Detections: diaSources

We cross-match to the truth catalog in two independent steps. First, we use the diaSource catalog as a reference and find the closest true SN location on the image. Next, we use the true SN catalog as the reference and find the closest diaSource. Finally, we compare these two sets of matches and define a True Positive Match (TP) if there is mutual agreement in both matches and their separation is below 0″.5. If a true SNIa does not match a diaSource, we flag it as a False Negative (FN).

From this procedure, we find a total of 17,719 matches, spanning a wide range of S/N and true magnitudes in all six filters. For the bias correction simulation, we measure the detection efficiency ($\epsilon = TP/(TP + FN)$) as a function of S/N and characterize this efficiency distribution with $S/N_{1/2}$ defined as $\epsilon(S/N_{1/2}) = 0.5$. To better connect the measured $\epsilon$ to simulations, we do not use measured S/N, but instead we compute S/N from the true flux and the true noise, where the latter is computed from the zero-point, PSF, and sky noise (see Equation (11) in Kessler et al. 2019).

**Table 2**
Mean and rms for Properties of Images Used for Template Co-addition and for DIA Season Images

| Set | Property | Statistic | $u$ | $g$ | $r$ | $i$ | $z$ | $y$ |
|---|---|---|---|---|---|---|---|---|
| Template | $m_{5\sigma}$ | mean | 24.94 | 26.24 | 25.69 | 25.03 | 24.25 | 23.23 |
| | | rms | 0.11 | 0.14 | 0.16 | 0.09 | 0.14 | 0.05 |
| | PSF | mean | 1.03 | 0.76 | 0.72 | 0.71 | 0.78 | 1.06 |
| | [FWHM, arcsec.] | rms | 0.03 | 0.06 | 0.03 | 0.02 | 0.03 | 0.02 |
| DIA seasons | $m_{5\sigma}$ | mean | 23.89 | 24.82 | 24.22 | 23.59 | 22.66 | 21.80 |
| | | rms | 0.18 | 0.22 | 0.27 | 0.31 | 0.25 | 0.15 |
| | PSF | mean | 0.96 | 0.95 | 0.90 | 0.87 | 0.98 | 1.21 |
| | [FWHM, arcsec.] | rms | 0.14 | 0.17 | 0.16 | 0.15 | 0.15 | 0.13 |
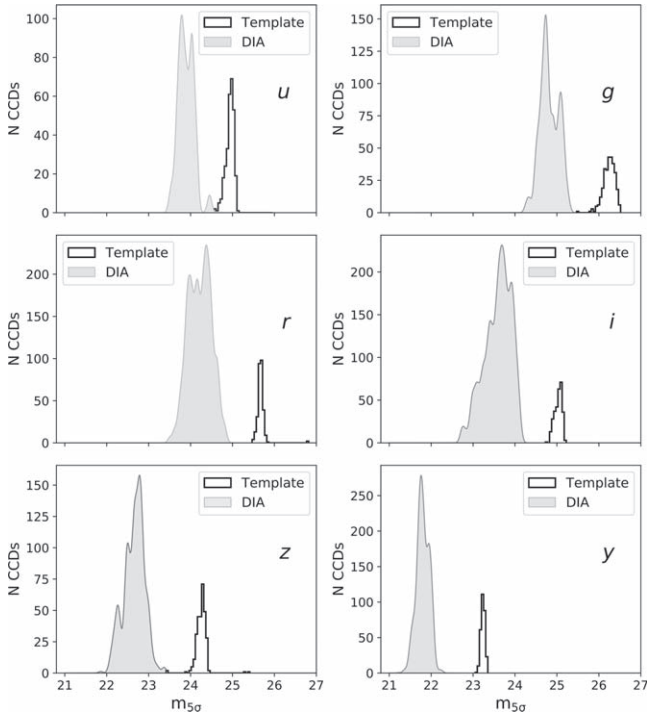


**Figure 6.** The $m_{5\sigma}$ distribution for templates, and for visits corresponding to DIA seasons.



**Figure 7.** PSF size distribution for template co-adds (dashed histogram), year 1 (histogram), and DIA season visits (years 2–5, smooth shaded curve), for each LSST filter. The right $y$-axis corresponds to template distribution. For *grizy*, the average template seeing is smaller than for the DIA seasons; for $u$ band the average template seeing is larger.

We estimate the value for $S/N_{1/2}$ by fitting a *sigmoid* function, $\epsilon = (1 + e^{-S/N})^{-1}$. Figure 9 shows $\epsilon(S/N)$ for all filters combined; $\epsilon$ increases with S/N as expected, and the filter-averaged $S/N_{1/2} = 5.82$. We also estimate $\epsilon$ as a function of magnitude for each bandpass as shown in Figure 10, which shows a clear correlation with $5\sigma$ limiting magnitudes (see Figure 6). For each LSST filter, $S/N_{1/2}$ and $m_{1/2}$ are listed in Table 3. The $S/N_{1/2}$ values are between 5.5 and 6 in each band. The $m_{1/2}$ values range from 21.6 in $y$ band to >24 in the $g$ and $r$ bands.

### 5.2. Artifact Contamination Level

To quantify the number of detected artifacts from DIA, we first match diaSource detections to all transients in the DC2 truth catalog, using a tolerance of $1''$. We define artifacts as unmatched diaSources. Using two bins in PSF seeing size for each filter, Table 4 shows the number of diaSource detections, number of matches, and number of artifacts. We show the number of matches for all true astrophysical variables ($N_{\text{diaSrc}}^{\text{var}}$) and true SNeIa ($N_{\text{diaSrc}}^{\text{SN}}$), along with the percentage of the total number of diaSources detections.

We characterize artifacts by computing the mean and rms of the density per square degree ($D_{\text{art}}$). $D_{\text{art}}$ is larger for images with smaller PSF and may in part be due to increased depth for smaller PSF. This effect is most pronounced in $u$ band: $D_{\text{art}} \sim 2000$ for PSF > $1''$, and it increases to ~4000 for PSF < $1''$. In $g$ band, $D_{\text{art}} \sim 1000$ with a 20% difference between the PSF bins. $D_{\text{art}}$ falls with increasing wavelength and is correlated with search depth; in $y$ band, $D_{\text{art}} \sim 300$ and the PSF difference is <10%. From Table 4, ~90% of the diaSource detections are artifacts in the *grizy* bands; in $u$ band the artifact fraction is 99% owing to template seeing size, which is relatively broader than search image PSF size. In previous surveys, machine-learning (ML) methods have significantly reduced artifacts (Goldstein et al. 2015; Kessler et al. 2015; Mahabal et al. 2019), and similar methods are under development within LSST.
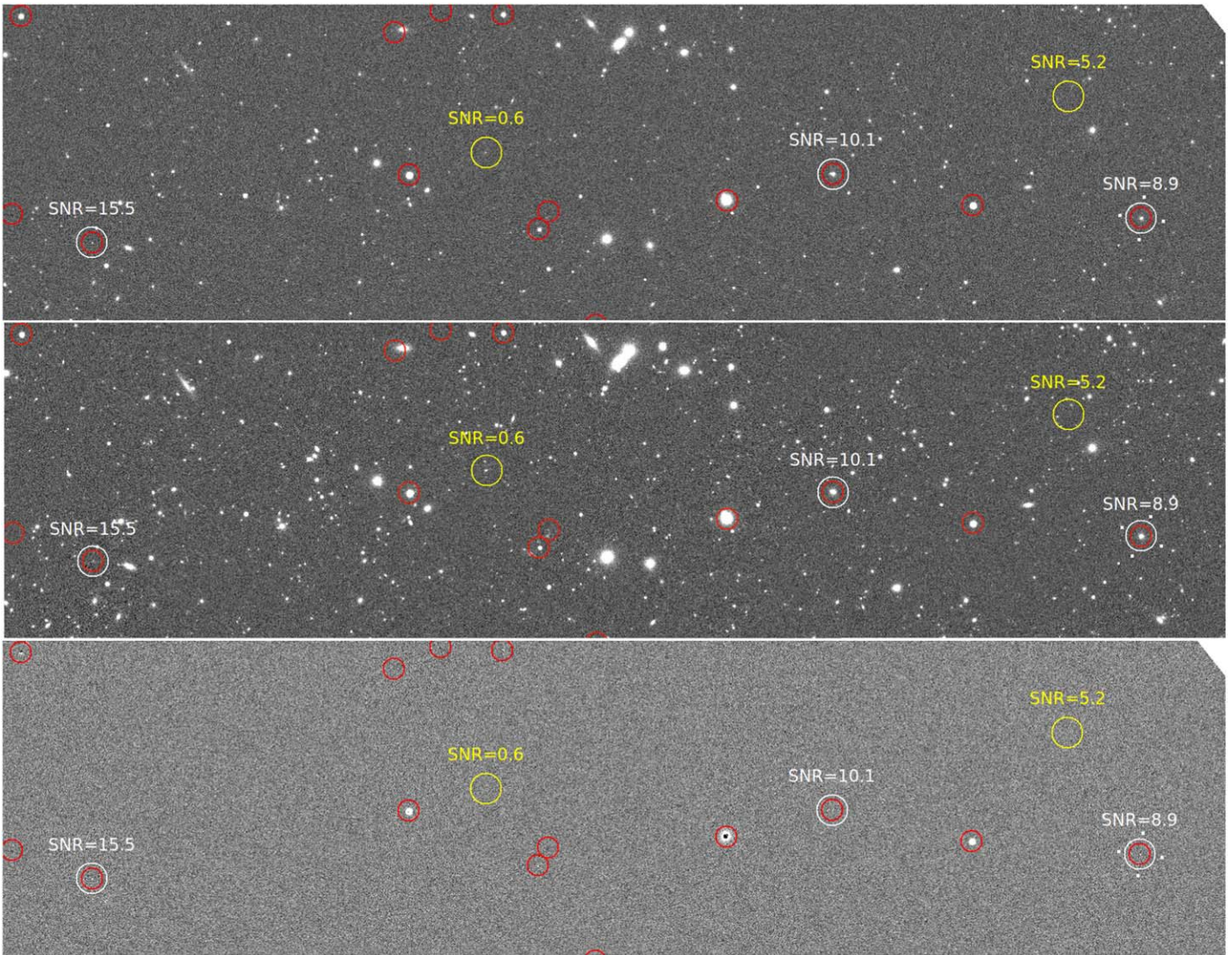
**Figure 8.** Example DIA *calexp* image (top), template image (middle), and difference image (bottom) from `dia_pipe`. Red circles show `diaSource` detections, white circles show found transients, and yellow circles show missed transients. On top of the circles we include the S/N value of each true transient point source.
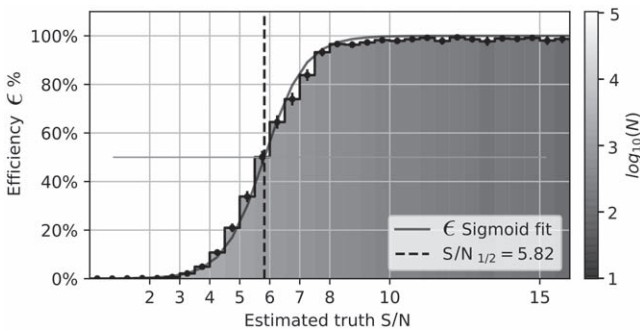


**Figure 9.** Detection efficiency ($\epsilon$) vs. calculated S/N. The color scale shows the number of objects per bin, and the dashed vertical line shows $S/N_{1/2}$.



**Figure 10.** Detection efficiency vs. true magnitude (0.2 mag bins) for each bandpass. Open circles indicate the intersection of the fitted sigmoid function for the efficiency and the 50% horizontal line, marking the value of $m_{1/2}$ for each bandpass.

### 5.3. DIA on Multiple Detections: `diaObjects`

We cross-match the `diaObject` catalog with the true DC2 SNeIa using a two-step procedure (as explained in Section 5.1) with a tolerance radius of 0″.5, finding a total of 2186 matched SNe. Figure 2 shows the DC2-SNIa area and true SNe that were matched and not matched to a `diaObject`. We define SN detection efficiency ($\epsilon_{SN}$) as the probability of associating a

**Table 3**
Measured $S/N_{1/2}$ and $m_{1/2}$ versus Filter

| Property | $u$ | $g$ | $r$ | $i$ | $z$ | $y$ |
|---|---|---|---|---|---|---|
| $S/N_{1/2}$ | 5.76 | 5.57 | 5.87 | 5.84 | 5.59 | 5.60 |
| $m_{1/2}$ | 23.66 | 24.69 | 24.06 | 23.45 | 22.54 | 21.62 |

8

**Table 4**
Number of `diaSources` Detections for SN and Artifacts, Split into Two PSF Bins

| Filter | $N_{CCD}$ [a] | PSF (arcsec) | $\overline{PSF}$ | $N_{diaSrc}$ [b] | $N_{diaSrc}^{SN}$ [c] | $N_{diaSrc}^{var}$ [d] | $N_{diaSrc}^{art}$ [e] | $\overline{D_{art}}$ (deg$^{-2}$) | $\sigma_{D_{art}}$ |
|---|---|---|---|---|---|---|---|---|---|
| $u$ | 3901 | >1.0 | 1.1 | 138,4171 | 61 (<0.01%) | 6298 (0.5%) | 137,7812 (99.5%) | 2190 | 3092 |
|  | 3902 | <1.0 | 0.9 | 299,9820 | 71 (<0.01%) | 7815 (0.3%) | 299,1934 (99.7%) | 4189 | 6620 |
| $g$ | 5870 | >1.0 | 1.1 | 411,704 | 692 (0.17%) | 41423 (10.1%) | 369,589 (89.8%) | 956 | 372 |
|  | 5870 | <1.0 | 0.8 | 502,003 | 922 (0.18%) | 53411 (10.6%) | 447,670 (89.2%) | 1207 | 453 |
| $r$ | 13905 | >0.9 | 1.0 | 743,402 | 3146 (0.42%) | 76986 (10.4%) | 663,276 (89.2%) | 725 | 244 |
|  | 13852 | <0.9 | 0.8 | 823,973 | 3679 (0.45%) | 90830 (11.0%) | 729,464 (88.5%) | 841 | 288 |
| $i$ | 14346 | >0.8 | 1.0 | 652,462 | 2695 (0.41%) | 70934 (10.9%) | 578,835 (88.7%) | 614 | 227 |
|  | 13495 | <0.8 | 0.7 | 724,098 | 3472 (0.48%) | 76858 (10.6%) | 643,768 (88.9%) | 736 | 250 |
| $z$ | 7375 | >1.0 | 1.0 | 279,164 | 361 (0.13%) | 30040 (10.8%) | 248,764 (89.1%) | 497 | 189 |
|  | 6579 | <1.0 | 0.9 | 292,950 | 491 (0.17%) | 31543(10.8%) | 260,916 (89.1%) | 591 | 227 |
| $y$ | 8533 | >1.2 | 1.3 | 177,009 | 66 (0.04%) | 20275 (11.5%) | 156,668 (88.5%) | 293 | 115 |
|  | 8105 | <1.2 | 1.1 | 177,733 | 68 (0.04%) | 22226 (12.5%) | 155,439 (87.5%) | 312 | 122 |

**Notes.**
[a] Number of CCD images.
[b] Number of `diaSource` detections.
[c] Number of `diaSources` matching with SNe (and percentage relative to `diaSources`).
[d] Number of `diaSources` matching with other variable sources (and percentage relative to `diaSources`).
[e] Number of artifacts (and percentage relative to `diaSources`).
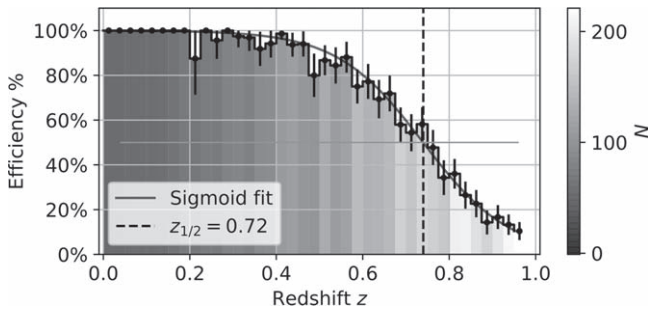


**Figure 11.** $\epsilon_{SN}$ vs redshift. The dashed vertical line shows where $\epsilon_{SN} = 0.5$. Gray color scale reflects the number of events per bin.



**Figure 12.** Mean fractional photometric bias, $F/F_{true} - 1$, as a function of true SN magnitude. Error bars show uncertainty on the mean, and solid gray lines show the standard deviation ($\pm 1\sigma$) in each bin, as well as the $\pm 1\%$ margin. The shaded area shows bins with less than 20 epochs per bin (a total of 75 observations); these epochs are all from seven SNe.

true SNIa with a `diaObject`. Figure 11 shows $\epsilon_{SN}$ versus redshift for a subsample of true SNeIa that have been observed more than 5 times, have at least one observation before $t_0$, and have at least one observation after $t_0 + 10$ days in the rest frame. Fitting this distribution to a sigmoid model (as in Section 5.1), $\epsilon_{SN} = 0.5$ at $z = 0.72$.

### 5.4. DIA Photometry: Flux Measurements

Forced PSF photometry is measured at the `diaObject` location on all DIA images. Using the set of `diaObjects` matched with DC2 SNe, we measure flux and magnitude residuals. Figure 12 shows the fractional photometric bias as a function of true SN magnitude ($m_{true}$), and the rms in each bin is illustrated by the $\pm 1\sigma$ envelope. The shaded region shows low-statistics bins with 20 observations but only seven events. While there is a hint of bias for bright events, note that correlated residuals among observations from the same event would result in underestimated uncertainties. We accurately measure fluxes for $19 < m_{true} < 23.25$, where the mean fractional photometric bias values are <1%. For magnitudes $m_{true} > 23.25$ the photometry is biased toward faint values, suggesting a slight bias in the sky subtraction.
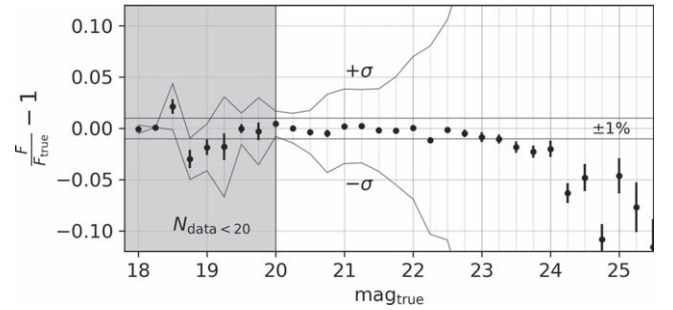
### 5.5. DIA Photometry: Flux Uncertainties

To evaluate the flux uncertainties, we measure the pull distribution in each band (Figure 13), $(F - F_{true})/\sigma_F$, where $F$ is the forced photometry flux, $\sigma_F$ is the uncertainty, and $F_{true}$ is the true flux. Defining

$$\text{rms}_{pull} \equiv \text{rms}[(F_{true} - F)/\sigma_F],  \quad (1)$$

we expect $\text{rms}_{pull} = 1$ if the uncertainties are accurate. We find that the distributions are nearly Gaussian, but $\text{rms}_{pull} > 1$. For $u$-band $\text{rms}_{pull} \sim 1.5$, indicating a significant underestimate of the flux uncertainties. For the other bands, $\text{rms}_{pull} \sim 1.1$.

For DES, Kessler et al. (2015) reported a "Surface Brightness (SB) anomaly" in which the true scatter was larger than the reported uncertainties, and this effect was strongly correlated with SB at the SN location. Here we repeat this analysis for DC2 and measure the local surface brightness magnitude ($m_{SB}$) in template co-adds at each SN location, using aperture photometry with a radius of $0\farcs9$. We find that the SB anomaly is present in DC2 simulated images. Figure 14 shows $\text{rms}_{pull}$ versus $m_{SB}$ for each filter. The $\text{rms}_{pull}$ is near 1 for faint SB and increases with increasing SB for *grizy* bands.
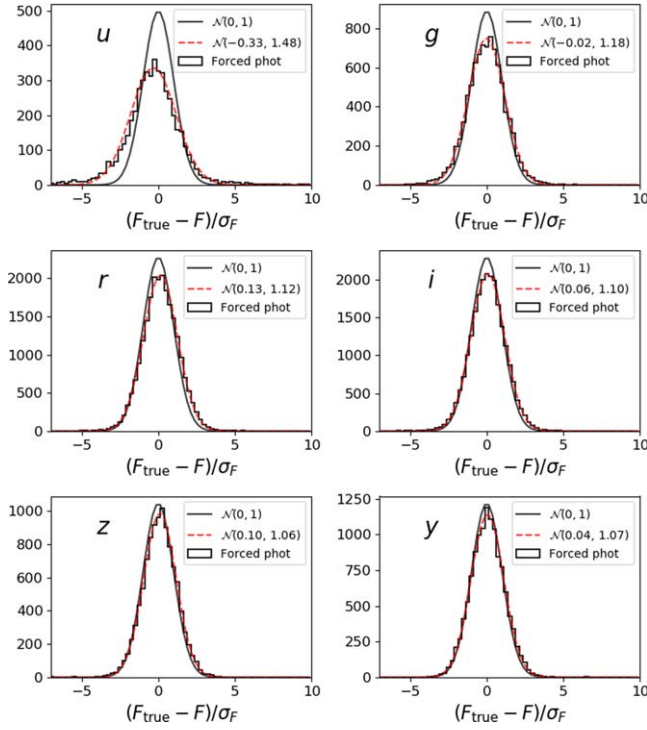
**Figure 13.** Distribution of forced photometry pull values as described in the text. The red curve shows the best-fit Gaussian model, and the black curve is a zero-mean unit dispersion normal distribution for comparison.
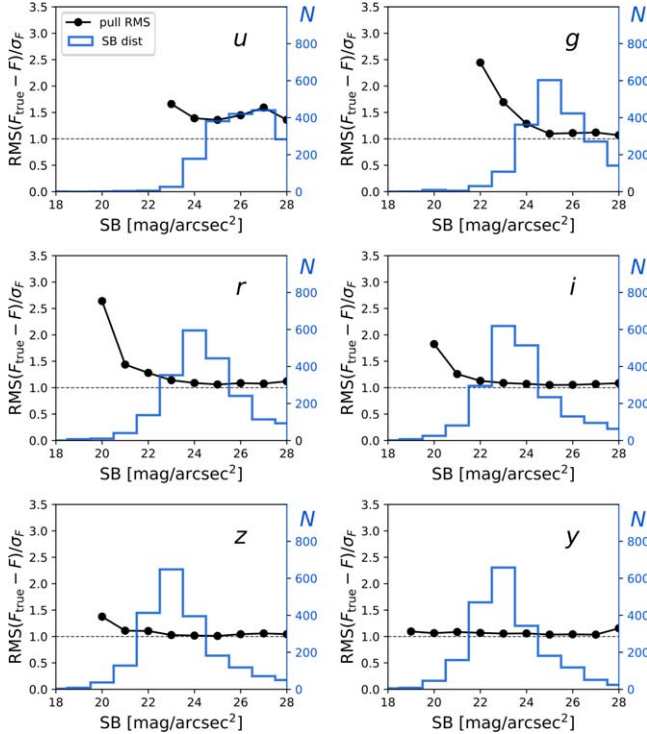


**Figure 14.** The rms of forced photometry pull as a function of $m_{SB}$ at the location of each SN. The dashed line shows the unit dispersion reference. The distribution of $m_{SB}$ is also shown for each band.

For $u$ band, $\mathrm{rms_{pull}} \sim 1.5$ for all $m_{SB}$. The $\mathrm{rms_{pull}}$ reaches a maximum of $\sim 3$ in the $g$ and $r$ bands with $m_{SB} \sim 21$ and $m_{SB} \sim 20$ mag, respectively. The $\mathrm{rms_{pull}}$ values are consistent for SNe of all peak brightness. This effect is not understood, and we therefore apply an empirical scale correction

**Table 5**
Flux Pull Distribution Parameters

| Filter | $N$ | $\bar{x}$[a] | $\mathrm{rms_{pull}}$ | $f_{5\sigma}$ (%)[b] | $f_{10\sigma}$ (%)[c] |
|--------|------|--------|------|------|------|
| $u$ | 3936 | −0.35 | 1.48 | 4.9 | 2.0 |
| $g$ | 8480 | −0.03 | 1.18 | 0.24 | 0.09 |
| $r$ | 22,366 | 0.15 | 1.12 | 0.22 | 0.05 |
| $i$ | 22,530 | 0.06 | 1.10 | 0.16 | 0.04 |
| $z$ | 10,221 | 0.10 | 1.06 | 0.06 | 0.01 |
| $y$ | 11,892 | 0.05 | 1.07 | 0.07 | 0.02 |

**Notes.**
[a] Robust mean of the pull.
[b] Percent of $5\sigma$ outliers.
[c] Percent of $10\sigma$ outliers.

**Table 6**
Number of Light Curves of Events from the DC2 Data That Pass Subsequent Cuts Prior to the Cosmological Analysis

| Selection Cut | Pass Cut | Fraction |
|---------------|----------|----------|
| At least a detection in any filter | 2182 | ⋯ |
| At least one observation before $t_0$ | 2012 | 92.2% |
| At least one observation 10 days after $t_0$ | 1843 | 84.5% |
| Max. S/N > 4 in at least three filters | 699 | 34.1% |
| Fitted $|x_1| < 3$, and $0 < \sigma_{x_1} < 2$ | 567 | 26.0% |
| Fitted $|c| < 0.3$ | 556 | 25.5% |
| Fitted peak MJD uncertainty <3 days | 550 | 25.1% |
| Fit probability $P_{fit} > 0.05$ | 526 | 24.1% |
| Valid bias correction in BBC | 504 | 23.1% |

(Figure 14) to the flux uncertainties. Comparisons with DES are presented in Section 6.

We show in Table 5 the robust mean and $\mathrm{rms_{pull}}$ for each filter flux pull distribution, as well as the percent of $5\sigma$ and $10\sigma$ outliers. The $u$-band outlier fraction ($\sim 1\%$) is roughly an order of magnitude higher than in the other bands. We found $u$-band bias and $\mathrm{rms_{pull}}$ to be anticorrelated with PSF size; the smallest PSF bin has the largest bias and $\mathrm{rms_{pull}}$.

### 5.6. Cosmology Analysis Results

Following the steps for cosmology analysis described in Section 3.3 and shown visually in Figure 3, we apply the selection requirements and fit light curves with the SALT2 light-curve model. Table 6 shows the number and fraction of events that pass each sequential cut; a total of 655 events pass cuts (504 for DC2, and 151 for SimLow-z).

We also create two catalog-level simulations that have the same DC2/SimLow-z proportion as the data and undergo the same cuts and light-curve fitting as the data: (1) a DATA-like simulation with 2061 events (1560 for DC2 and 501 for SimLow-z) is used to compare data-sim distributions and to cross-check the analysis, and (2) a large ($6.8 \times 10^5$ events) bias correction simulation is used in BBC. The difference between the two simulations is that the latter is generated on a $2 \times 2$ grid of $\alpha$ and $\beta$ to enable interpolating the bias correction during the BBC fit.

Since the SimLow-z sample is generated by the same catalog simulation used for bias correction, there is no need to validate this bias correction. However, it is important to validate the bias correction for DC2 by comparing several distributions between the DC2 data and the DATA-like simulation: the
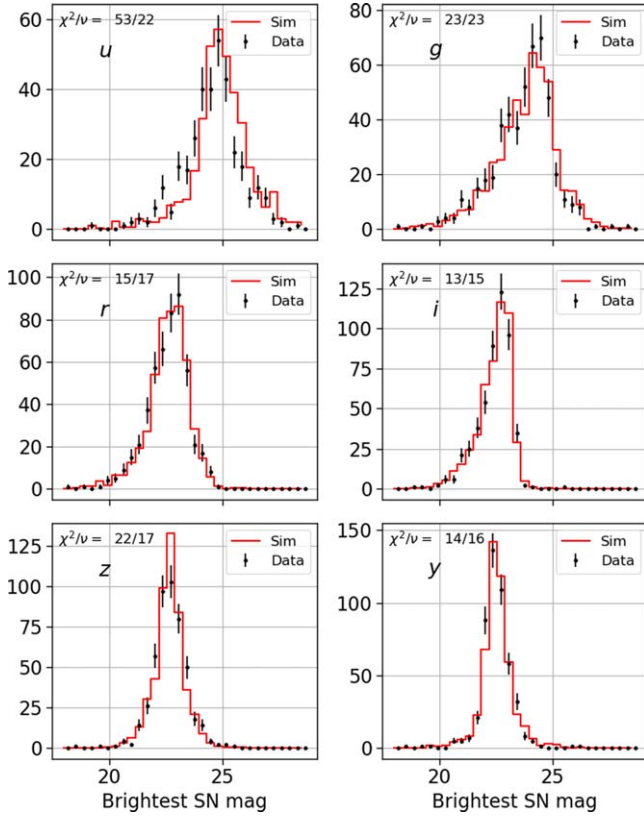
**Figure 15.** Distribution of brightest observed magnitude in each filter for DC2 data (black circles) and DATA-like simulation (red histogram). Each simulated distribution is scaled to match the DC2 sample size. The $\chi^2$ per degrees of freedom ($\nu$) quantifies the data-sim agreement.
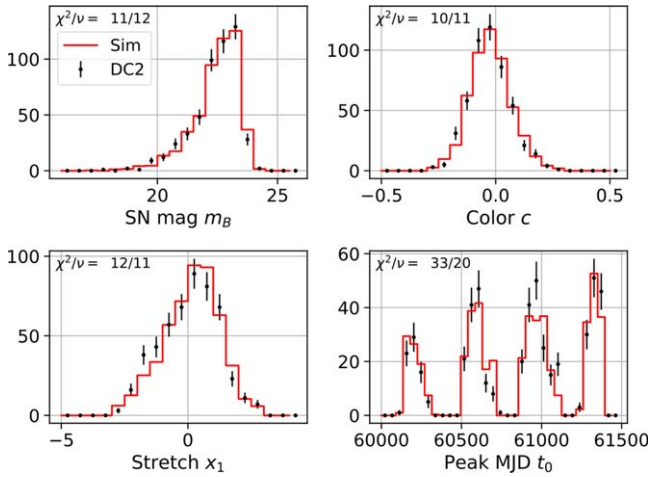


**Figure 16.** Distribution of SALT2 fit parameters for DC2 data (black circles) and DATA-like simulation (red histogram). Each simulated distribution is scaled to match the DC2 sample size. The $\chi^2$ per degrees of freedom ($\nu$) quantifies the data-sim agreement.



**Figure 17.** Detection efficiency vs. redshift in DC2 data (black solid curve) and in DATA-like simulation (red solid curve). Analysis efficiency vs. redshift for events satisfying cuts and SALT2 fits in DC2 data (black dashed curve) and in DATA-like simulation (red dashed curve).
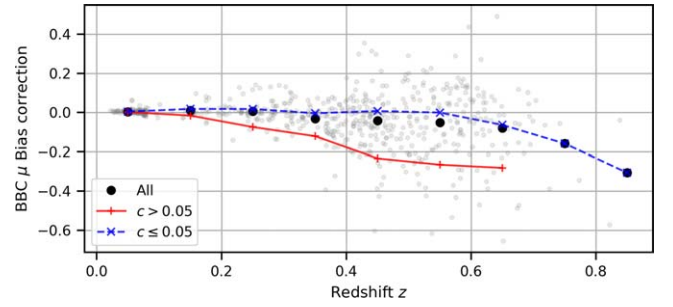


**Figure 18.** Average DC2 bias correction vs. redshift for BBC fitted distances. Black circles are for all events, the blue curve is for fitted SALT2 color $c < 0.05$, and the red curve is for $c > 0.05$.
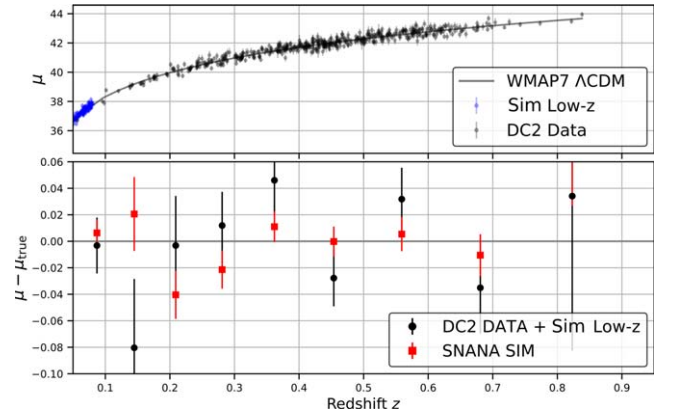


**Figure 19.** Bias-corrected Hubble diagram for DC2 data (top) and redshift-binned Hubble residuals for DC2 data and DC2-like simulation (bottom).

observed magnitude for the brightest flux in each filter (Figure 15), and SALT2 fit parameters (Figure 16). All distributions show excellent agreement except for brightest $u$-band magnitude in Figure 15.

In Figure 17 we compare the DC2 detection efficiency versus redshift, as well as the analysis efficiency versus redshift using the requirements listed in Section 3.3. Fitting a sigmoid function to the detection efficiency curves, $z_{1/2} = 0.730 \pm 0.0051$ for DC2

data, and $z_{1/2} = 0.730 \pm 0.003$ for the DATA-like simulation. For the analysis efficiency, $z_{1/2} = 0.58 \pm 0.02$ for DC2 data, and $z_{1/2} = 0.61 \pm 0.01$ for the DATA-like simulation.

The distance bias correction for SimLow-z averages to zero, with small $\sim 0.01$ mag fluctuations. For DC2, the distance bias correction versus redshift is shown in Figure 18 for all events (black circles), where the average bias increases rapidly for $z > 0.6$. The subset of blue ($c < 0.05$) events, which are brighter than average, has a smaller bias in the intermediate redshift range. The fainter subset of red ($c \leqslant 0.05$) events has a much larger bias at lower redshifts. Accurate simulations and bias corrections are essential for the cosmology analysis.

**Table 7**
Bias-corrected Parameter Estimation for DC2 Sample and Simulations

| Data Set | $N_{\text{Events}}$ | From Cosmology Fit | | | From BBC Fit | | |
| --- | --- | --- | --- | --- | --- | --- | --- |
| | | $\Delta w = w - w_{\text{true}}$ | $\Delta\Omega_M = \Omega_M - \Omega_M^{\text{true}}$ | $\chi^2/\nu$ | $\Delta\alpha = \alpha - \alpha_{\text{true}}$ | $\Delta\beta = \beta - \beta_{\text{true}}$ | $\sigma_{\text{int}}/\sigma_{\text{int}}^{\text{true}}$ |
| DC2+SimLow-z | 655 | $-0.032 \pm 0.046$ | $-0.007 \pm 0.013$ | 11/8 | $-0.004 \pm 0.010$ | $-0.15 \pm 0.14$ | 1.02 |
| DATA-like Sim | 2061 | $-0.002 \pm 0.026$ | $0.001 \pm 0.009$ | 12/8 | $0.004 \pm 0.005$ | $-0.12 \pm 0.06$ | 0.94 |

For the full DC2+SimLow-z sample, Figure 19 shows the bias-corrected Hubble diagram and the Hubble residuals with respect to the reference DC2 cosmology, for both DC2+SimLow-z data and DATA-like simulation. Using nine bins of redshift, we estimate mean Hubble residuals and error on the mean, shown in the bottom panels of Figure 19; the binned residuals are <0.04 mag and consistent with 0, and no clear trend is seen with redshift. Our redshift binning has no impact in our results because we have not used a systematic covariance matrix in our analysis (Brout et al. 2021).

After applying the bias correction analysis to the DATA-like simulation, we measure nuisance and cosmological parameters. Defining the bias on $x$ as $\Delta x \equiv x - x_{\text{true}}$, the biases with respect to input values (Table 1) are shown in the "DATA-like Sim" row of Table 7, and these biases are consistent with zero: $\Delta w = -0.002 \pm 0.026$ and $\Delta\Omega_M = 0.001 \pm 0.009$. After this validation, we apply the same treatment to DC2+SimLow-z data and obtain nuisance and cosmological parameters (DC2 row in Table 7). We find $\Delta w = -0.032 \pm 0.046$ and $\Delta\Omega_M = -0.007 \pm 0.013$. The nuisance and cosmological parameter biases are consistent with zero.

### 5.6.1. u-band Shift

We studied the impact on our cosmology analysis from excluding $u$-band photometry. A total of 16 events (3% of sample) are recovered, and the change in $w$ is $\Delta w_{\text{DC2}} = 0.027$. To estimate the significance of this shift, we created 31 independent simulated light-curve samples and ran a full cosmology analysis to obtain $w$ in two modes: (1) using the six $ugrizy$ filters, and (2) excluding $u$ band ($grizy$). We measure the $w$-shift for each simulated sample and obtain a mean value of $\mu_{\Delta w} = -0.0003$ and a dispersion of $\sigma_{\Delta w} = 0.012$. The ratio $(\Delta w_{\text{DC2}} - \mu_{\Delta w})/\sigma_{\Delta w} \sim 2.3$, and thus the chance of having a shift similar to $\Delta w_{\text{DC2}}$ due to random fluctuations is around 2%, which translates to a significant $w$-shift when dropping $u$ band.

## 6. Discussion

Our DIA performance study is similar to that in Kessler et al. (2015) for the Dark Energy Survey (DES), where they used fake light curves injected onto real images during DES operations. In Table 8 we compare several difference-image properties for DC2 and DES. To avoid confusion related to different search depths, we only compare DES bands with similar DC2 depth in Table 3: DES $g$ band in their deep fields ($m_{1/2} \sim 24.5$ mag) and DES $i$ band in their shallow fields ($m_{1/2} \sim 23.5$ mag).

For S/N at 50% detection efficiency, the $\text{S/N}_{1/2}$ values are almost identical in $g$ band, while the DES $i$-band value is $\sim 10\%$ smaller. To compare the excess scatter on bright galaxies, we evaluate the SB magnitude where the flux uncertainty scale factor is 2: $m_{\text{SB}}(\text{rms}_{\text{pull}} = 2)$. These $m_{\text{SB}}$

**Table 8**
Difference-image Properties for DC2 and DES

| | DC2-$g$ | DES-$g$[a] | DC2-$i$ | DES-$i$[b] |
| --- | --- | --- | --- | --- |
| $m_{1/2}$ | 24.7 | 24.5 | 23.5 | 23.5 |
| $\text{S/N}_{1/2}$ | 5.57 | 5.61 | 5.84 | 5.36 |
| $m_{\text{SB}}(\text{rms}_{\text{pull}} = 2)$ | 22.1 | 22.0 | 19.8 | 21.5 |
| $\overline{D}_{\text{art}}$ | 1080 | 520 | 680 | 730 |
| $f_{5\sigma}(\%)$ | 0.24 | 0.49 | 0.16 | 0.25 |
| $f_{10\sigma}(\%)$ | 0.09 | 0.09 | 0.04 | 0.06 |

**Notes.**
[a] From DES SN Deep fields, to match DC2-$g$ depth.
[b] From DES SN Shallow fields, to match DC2-$i$ depth.

**Table 9**
$m_{\text{SB}}(\text{rms}_{\text{pull}} = 2)$[a] for Each DC2 Band

| $u_{\text{SB}}$ | $g_{\text{SB}}$ | $r_{\text{SB}}$ | $i_{\text{SB}}$ | $z_{\text{SB}}$ | $y_{\text{SB}}$ |
| --- | --- | --- | --- | --- | --- |
| _[b] | 22.1 | 20.5 | 19.8 | 19[c] | …[b] |

**Notes.**
[a] Surface brightness [mag/arcsec$^2$] where flux uncertainty scale is $\sim 2$.
[b] Scale is always $< 2$.
[c] Estimated from extrapolation.

values are nearly identical in $g$ band (22.1 and 22.0 mag for DC2 and DES, respectively) but differ by 1.7 mag in $i$ band (19.8 and 21.5 mag); the origin of this difference is not understood. The $m_{\text{SB}}(\text{rms}_{\text{pull}} = 2)$ values for all DC2 bands are shown in Table 9. The number of detection artifacts per deg$^2$ is also similar; DC2 is a factor of 2 higher for $g$ band and 7% smaller in $i$ band. Finally, the $5\sigma$ flux-outlier fractions for DC2 are about a factor of 2 smaller compared to DES; the corresponding $10\sigma$ outlier fractions are much more similar. Assessing the overall performance, DC2 appears to be slightly better because of the improved $m_{\text{SB}}(\text{rms}_{\text{pull}} = 2)$ in the $i$ band and the reduced $5\sigma$ flux outliers. While this DC2-versus-DES comparison is encouraging for `dia_pipe`, the processing of simulated DC2 images may be giving somewhat optimistic results compared to real data.

The SB anomaly is present in both DES and DC2 but still not understood. Our comparison between both surveys of $m_{\text{SB}}(\text{rms}_{\text{pull}} = 2)$ shows agreement in $g$ band and a large discrepancy in $i$ band. Follow-up to DC2 simulations would enable modifying various atmospheric or detector effects to trace the origin of the anomaly. Improving DIA is important for studies of transients near cores of bright galaxies.

A similar DIA efficiency study was done by the Palomar Transient Factory (PTF; Frohmaier et al. 2017) using $\sim 7$ million artificial point sources overlaid on PTF images. They characterized their real-time detection efficiency as a

function of source magnitude, host galaxy surface brightness, and various observing conditions. Their efficiencies are mostly parameterized by surface brightness and thus cannot be directly compared with our DC2 results using S/N. Nevertheless, they report an $m_{1/2} \simeq 20.3$ in $R$ band for a PTF 48-inch class instrument. As shown in DES, PTF, and this DC2 analysis, the detection efficiency has not been analytically modeled and was therefore determined empirically with fake sources.

DIA performance depends critically on using template images with exceptional quality, in particular a narrower PSF with respect to search images. We created templates using Y1 data and found that poor $u$-band seeing in Y1 (Figure 7) degraded DIA for $u$ band, where we find a drop in detection efficiency, as well as biases in photometric flux and uncertainty. The $u$-band filter transmission is much lower than for the other bands, and it is unlikely to discover SNeIa because they are faint in the UV; nonetheless, $u$ band is useful for photometric classifiers to distinguish between SNeIa and core-collapse SNe. As an additional test we excluded $u$ band from our cosmology analysis and find a $w$-shift of $-0.027$ ($0.6\sigma$ change) for the DC2 sample. We have not traced the origin of this shift.

The level of artifact detections from DIA is consistent with DES (Table 8). ML methodologies are expected to reduce this contamination significantly, according to results obtained by several collaborations (Brink et al. 2013; Goldstein et al. 2015; Duev et al. 2019; Mahabal et al. 2019). We find that the density of artifact detections decreases with increasing PSF size in the search image. This effect might be caused by the DIA kernel transformation, which performs better when the search and template PSF difference becomes larger (S. Liu et al., in preparation).

The DC2 baseline cadence is suboptimal with respect to the recent developments in LSST cadence studies (Lochner et al. 2018; Scolnic et al. 2018c; Lochner et al. 2021). Repeating this DC2 image simulation and analysis on alternative cadences is impractical from both a computational and human-effort perspective. To rigorously evaluate alternative cadences, however, this DC2 analysis demonstrates that the SNANA simulation can rapidly generate light-curve samples that accurately model a full DIA analysis on images. The SNANA simulation uses metadata from images and DIA that includes cadence, zero-point, PSF, sky noise, detection efficiency versus S/N, and flux uncertainty versus SB. A recommended simulation upgrade is to model catastrophic flux outliers shown in Table 5.

## 7. Conclusions

In this work, we show results of an integrated DIA pipeline, built using DESC's dia_pipe and LSST pipelines, to analyze simulated images that include SNIa light curves. Using a light-curve catalog compiled from dia_pipe results, we applied a commonly used SNIa standardization method to measure cosmic distances and cosmological parameters. This is the first time that a survey team has carried out such a pixel-to-cosmology test before commissioning operations begin. This analysis is an important stepping stone, enabling monitoring of pipeline performance evolution from survey simulations to real-time analysis during operations.

We have analyzed 15 deg$^2$ of DC2 WFD images using LSST DESC's dia_pipe pipeline framework for difference imaging and transient discovery. The detection efficiency is

$\sim$100% for point sources with S/N $\geqslant 8$ and is 50% efficient for events with S/N $\sim 5.8$. Comparing DC2 and DES in bands with the same search depth, the difference-image properties are quite similar (Table 8). To the extent that the simulated DC2 images are realistic, this comparison shows that dia_pipe is already performing at the level of a stage III precursor survey that was focused on precision measurements of cosmological parameters.

We apply a cosmology analysis using a SALT2+BBC framework, resulting in 655 SNIa light curves (504 for DC2, 151 for SimLow-z). To correct for distance biases in BBC, we used SNANA to generate a DATA-like simulation of SN Ia light curves using measured DC2 image properties (PSF, zero-point, sky noise) and measured DIA properties (efficiency vs. S/N, flux uncertainty scale vs. SB). Both the DC2 and DATA-like simulated samples were used to measure $w$ and $\Omega_M$ from a bias-corrected Hubble diagram; in both cases we recovered the true cosmological and nuisance parameter values within statistical uncertainties.

We emphasize that the pipeline system is still in active development and may improve by the time LSST starts operations. The pre-commissioning analysis of DC2 is a central contribution for operational readiness.

### ORCID iDs

B. O. Sánchez ✦ https://orcid.org/0000-0002-8687-0669
R. Kessler ✦ https://orcid.org/0000-0003-3221-0419
D. Scolnic ✦ https://orcid.org/0000-0002-4934-5849
R. Armstrong ✦ https://orcid.org/0000-0002-6911-1038
R. Biswas ✦ https://orcid.org/0000-0002-5741-7195
J. Bogart ✦ https://orcid.org/0000-0002-1345-1359
J. Chiang ✦ https://orcid.org/0000-0001-5738-8956
J. Cohen-Tanugi ✦ https://orcid.org/0000-0001-9022-4232
D. Fouchez ✦ https://orcid.org/0000-0002-7496-3796
Ph. Gris ✦ https://orcid.org/0000-0001-5673-0959
K. Heitmann ✦ https://orcid.org/0000-0003-1468-8232
R. Hložek ✦ https://orcid.org/0000-0002-0965-7864
S. Jha ✦ https://orcid.org/0000-0001-8738-6011
H. Kelly ✦ https://orcid.org/0000-0002-4394-6192
S. Liu ✦ https://orcid.org/0000-0002-4461-2143
G. Narayan ✦ https://orcid.org/0000-0001-6022-0484
B. Racine ✦ https://orcid.org/0000-0001-8861-3052
E. Rykoff ✦ https://orcid.org/0000-0001-9376-3135
M. Sullivan ✦ https://orcid.org/0000-0001-9053-4820
C. W. Walter ✦ https://orcid.org/0000-0003-2035-2380
W. M. Wood-Vasey ✦ https://orcid.org/0000-0001-7113-1233

### References

Abbott, T. M. C., Allam, S., Andersen, P., et al. 2019, ApJL, 872, L30
Ade, P. A., Aghanim, N., Arnaud, M., et al. 2016, A&A, 594, A13
Alard, C., & Lupton, R. H. 1998, ApJ, 503, 325
Astropy Collaboration, Price-Whelan, A. M., Sipőcz, B. M., et al. 2018, AJ, 156, 123
Astropy Collaboration, Robitaille, T. P., Tollerud, E. J., et al. 2013, A&A, 558, A33
Betoule, M., Kessler, R., Guy, J., et al. 2014, A&A, 568, A22
Brink, H., Richards, J. W., Poznanski, D., et al. 2013, MNRAS, 435, 1047
Brout, D., Hinton, S. R., & Scolnic, D. 2021, ApJL, 912, L26
Brout, D., Scolnic, D., Kessler, R., et al. 2019, ApJ, 874, 150
Dilday, B., Kessler, R., Frieman, J. A., et al. 2008, ApJ, 682, 262
Duev, D. A., Mahabal, A., Masci, F. J., et al. 2019, MNRAS, 489, 3582
Frohmaier, C., Sullivan, M., Nugent, P. E., Goldstein, D. A., & DeRose, J. 2017, ApJS, 230, 4
Goldstein, D. A., D'Andrea, C. B., Fischer, J. A., et al. 2015, AJ, 150, 82
Graham, M. L., Bellm, E., Guy, L., & Slater, C. T. 2020, LSST Alerts: Key Numbers, DMTN-102 LSST, https://dmtn-102.lsst.io
Guy, J., Sullivan, M., Conley, A., et al. 2010, A&A, 523, A7
Heitmann, K., Finkel, H., Pope, A., et al. 2019, ApJS, 245, 16
Hunter, J. D. 2007, CSE, 9, 90
Ivezić, Ž., Kahn, S. M., Tyson, J. A., et al. 2019, ApJ, 873, 111
Jones, D. O., Scolnic, D. M., Foley, R. J., et al. 2019, ApJ, 881, 19
Jones, D. O., Scolnic, D. M., Riess, A. G., et al. 2018, ApJ, 857, 51
Kessler, R., Brout, D., D'Andrea, C. B., et al. 2019, MNRAS, 485, 1171
Kessler, R., Marriner, J., Childress, M., et al. 2015, AJ, 150, 172
Kessler, R., & Scolnic, D. 2017, ApJ, 836, 56
Komatsu, E., Dunkley, J., Nolta, M. R., et al. 2009, ApJS, 180, 330
Komatsu, E., Smith, K. M., Dunkley, J., et al. 2011, ApJS, 192, 18
Korytov, D., Hearin, A., Kovacs, E., et al. 2019, ApJS, 245, 26
Lochner, M., Scolnic, D., Almoubayyed, H., et al. 2022, ApJS, 259, 58
Lochner, M., Scolnic, D. M., Awan, H., et al. 2018, arXiv:1812.00515
LSST Dark Energy Science Collaboration, Abolfathi, B., Alonso, D., et al. 2021, ApJS, 253, 31
LSST Science Collaboration, Abell, P. A., Allison, P., et al. 2009, arXiv:0912.0201
Mahabal, A., Rebbapragada, U., Walters, R., et al. 2019, PASP, 131, 038002
McKinney, W. 2010, in 9th Python in Science Conf., 445 (Austin, TX: SciPy), 51
Pierel, J. D. R., Rodney, S., Avelino, A., et al. 2018, PASP, 130, 114504
Rest, A., Scolnic, D., Foley, R. J., et al. 2014, ApJ, 795, 44
Ridgway, S. T., Matheson, T., Mighell, K. J., Olsen, K. A., & Howell, S. B. 2014, ApJ, 796, 53
Sako, M., Bassett, B., Becker, A. C., et al. 2018, PASP, 130, 064002
Sánchez, F. J., Walter, C. W., Awan, H., et al. 2020, MNRAS, 497, 210
Scolnic, D., Kessler, R., Brout, D., et al. 2018a, ApJL, 852, L3
Scolnic, D. M., Jones, D. O., Rest, A., et al. 2018b, ApJ, 859, 101
Scolnic, D. M., Lochner, M., Gris, P., et al. 2018c, arXiv:1812.00516
The LSST Dark Energy Science Collaboration, Mandelbaum, R., Eifler, T., et al. 2018, arXiv:1809.01669
The LSST Dark Energy Science Collaboration (DESC) 2019, LSST DESC Science Roadmap, Zenodo, doi:10.5281/ZENODO.3547567
van der Walt, S., Colbert, S. C., & Varoquaux, G. 2011, CSE, 13, 22
Virtanen, P., Gommers, R., Oliphant, T. E., et al. 2020, NatMe, 17, 261
Waskom, M., Botvinnik, O., Hobson, P., et al. 2014, seaborn: v0.5.0 , Zenodo, doi:10.5281/zenodo.12710